

Morpho-Photometric Classification of KiDS DR5 Sources Based on Neural Networks: A Comprehensive Star-Quasar-Galaxy Catalog

HAI-CHENG FENG,^{1,2,3,4} RUI LI,⁵ NICOLA R. NAPOLITANO,^{6,7,8} SHA-SHA LI,^{1,2,3,4} J. M. BAI,^{1,2,3,4} RAN LI,^{9,10} H. T. LIU,^{1,2,3}
KAI-XING LU,^{1,2,3} MARIO RADOVICH,¹¹ HUAN-YUAN SHAN,¹² JIAN-GUO WANG,^{1,2,3} WEN-ZHE XI,^{1,9} LING-HUA XIE,⁶ AND
YANG-WEI ZHANG¹³

¹Yunnan Observatories, Chinese Academy of Sciences, Kunming 650216, Yunnan, People's Republic of China

²Key Laboratory for the Structure and Evolution of Celestial Objects, Chinese Academy of Sciences, Kunming 650216, Yunnan, People's Republic of China

³Center for Astronomical Mega-Science, Chinese Academy of Sciences, 20A Datun Road, Chaoyang District, Beijing 100012, People's Republic of China

⁴Key Laboratory of Radio Astronomy and Technology, Chinese Academy of Sciences, 20A Datun Road, Chaoyang District, Beijing 100101, People's Republic of China

⁵Institute for Astrophysics, School of Physics, Zhengzhou University, Zhengzhou, 450001, People's Republic of China

⁶School of Physics and Astronomy, Sun Yat-sen University, Zhuhai Campus, 2 Daxue Road, Xiangzhou District, Zhuhai, People's Republic of China

⁷CSST Science Center for Guangdong-Hong Kong-Macau Great Bay Area, Zhuhai, 519082, People's Republic of China

⁸INAF – Osservatorio Astronomico di Capodimonte, Salita Moiariello 16, 80131 - Napoli, Italy

⁹University of Chinese Academy of Sciences, Beijing 100049, People's Republic of China

¹⁰National Astronomical Observatories, Chinese Academy of Sciences, 20A Datun Road, Chaoyang District, Beijing 100012, People's Republic of China

¹¹INAF - Osservatorio Astronomico di Padova, via dell'Osservatorio 5, 35122 Padova, Italy

¹²Shanghai Astronomical Observatory, Chinese Academy of Sciences, Shanghai 200030, People's Republic of China

¹³South-Western Institute for Astronomy Research, Yunnan University, Kunming 650500, People's Republic of China

ABSTRACT

We present a novel multimodal neural network for classifying astronomical sources in multiband ground-based observations, from optical to near infrared, to separate sources in stars, galaxies and quasars. Our approach combines a convolutional neural network branch for learning morphological features from r -band images with an artificial neural network branch for extracting spectral energy distribution (SED) information. Specifically, we have used 9-band optical ($ugri$) and NIR ($ZYHJK_s$) data from the Kilo-Degree Survey (KiDS) Data Release 5. The two branches of the network are concatenated and feed into fully-connected layers for final classification. We train the network on a spectroscopically confirmed sample from the Sloan Digital Sky Survey cross-matched with KiDS. The trained model achieves 98.76% overall accuracy on an independent testing dataset, with F1 scores exceeding 95% for each class. Raising the output probability threshold, we obtain higher purity at the cost of a lower completeness. We have also validated the network using external catalogs cross-matched with KiDS, correctly classifying 99.74% of a pure star sample selected from Gaia parallaxes and proper motions, and 99.74% of an external galaxy sample from the Galaxy and Mass Assembly survey, adjusted for low-redshift contamination. We apply the trained network to 27,334,751 KiDS DR5 sources with $r \leq 23$ mag to generate a new classification catalog. This multimodal neural network successfully leverages both morphological and SED information to enable efficient and robust classification of stars, quasars, and galaxies in large photometric surveys.

Keywords: Neural networks(1933), Classification(1907), Surveys(1671), Catalogs(205), A stars(5), Quasars(1319), Galaxies(573)

1. INTRODUCTION

Stars, galaxies, and quasars are the three main categories of astronomical objects in most large scale surveys, enabling advances in our understanding of cosmic structure, evolution, and fundamental physics. Stars, the most observable entities in the universe, are the basic building blocks of galaxies. Systematic observations and cataloging of stars not only yield a wealth of information about stellar evolution and the synthesis of heavy elements, but also aid in mapping the structure and dynamics of the Milky Way (Helmi 2020; Zhang et al.

Corresponding author: Hai-Cheng Feng, Rui Li, & Nicola R. Napolitano

hcfeng@ynao.ac.cn

liruiww@gmail.com

nicolarosario.napolitano@unina.it

arXiv:2406.03797v1 [astro-ph.GA] 6 Jun 2024

2023). Galaxies, large assemblies of stars, gas, dust, and dark matter bound by gravity, serve as fundamental components of large-scale structure. A comprehensive census and analysis of galaxies can reveal the underlying distribution of dark matter and provide a platform for testing cosmological models that describe the origin and evolution of the Universe (Bond et al. 1996; Behroozi et al. 2013). Quasars, also known as quasi-stellar objects (QSOs), represent extremely luminous galactic nuclei fueled by matter accretion onto supermassive black holes. They serve as invaluable tools for probing the formation and evolution of supermassive black holes, and understanding their connection to their host galaxies (Schmidt 1963; Salpeter 1964; Kormendy & Ho 2013). Accurate classification of these diverse celestial objects stands as an indispensable prerequisite for conducting detailed follow-up studies and science analyses.

Over the course of several decades, extensive efforts have been devoted to develop various approaches for separating stars, QSOs, and galaxies. Spectroscopic observations are among the most reliable methods, primarily due to the unique physical properties of these three types of astronomical objects (e.g., Baldwin et al. 1981; Feng et al. 2021; Verro et al. 2022). The emergence of spectroscopic survey projects, such as the Sloan Digital Sky Survey (SDSS; York et al. 2000), the Large Sky Area Multi-Object Fiber Spectroscopic Telescope (LAMOST; Cui et al. 2012), and the Dark Energy Spectroscopic Instrument (DESI; DESI Collaboration et al. 2016), has enabled the collection of spectra for millions of targets. This has, in turn, led to the proposal of some automatic spectral classification methods, including the Baldwin-Phillips-Terlevich (BPT) diagnostic scheme (Baldwin et al. 1981) and template matching (Bolton et al. 2012). However, most spectroscopic surveys employ multi-object fiber spectrographs, which are limited to observing hundreds to thousands of targets concurrently, necessitating exposure times of several thousand seconds. This requires a significant amount of telescope time to obtain large statistical samples, but results in relatively shallow data for each target. As a result, target pre-selection is often implemented in these surveys, which can introduce bias in sample statistics and increase the likelihood of missing peculiar celestial populations.

As alternative to spectroscopy, multi-band imaging can effectively trace the impact of different radiative process in the spectral energy distributions (SEDs) of astronomical sources. In this case, source classification can be performed via color-color diagnostic (Richards et al. 2002; Peters et al. 2015) or SED fitting (Ilbert et al. 2009; Salvato et al. 2009). The photometric approach has the advantage to collect all targets under a limited brightness in the field of view, effectively eliminating any selection bias. In contrast to spectroscopic observation, photometry requires shorter exposure times, often just a few minutes, to reach deeper limiting magnitudes. Furthermore, image data can provide morphological details that are not accessible from spectra, which contains rich physical information. Indeed, the first attempt to perform object classifications, the primary methods were visual inspection of images or analysis of morphological parameters (e.g., Hub-

ble 1926; MacGillivray et al. 1976; Yee 1991; Scranton et al. 2002; Kelvin et al. 2014; López-Sanjuan et al. 2019). This technique proved to be effective in differentiating between stars (point sources) and galaxies (extended structures), and even enabled the identification of certain QSOs with notable host galaxies (Guo et al. 2022).

Ongoing wide-field imaging surveys provide continuous streams of multi-band photometric data, enabling the potential for obtaining complete samples of various celestial object. Current projects like the Hyper Suprime-Cam Subaru Strategic Program (HSC-SSP; Aihara et al. 2018), Dark Energy Survey (DES; The Dark Energy Survey Collaboration 2005), and Kilo Degree Square Survey (KiDS; de Jong et al. 2015) are amassing observations spanning hundreds of millions of targets. Upcoming programs, like the China Space Station Telescope (CSST; Gong et al. 2019), Large Synoptic Survey Telescope (LSST; Ivezić et al. 2019), and the Euclid mission (Laureijs et al. 2011), will dramatically escalate data volumes into billions or more. The wealth of data sets underscores the urgent need for rapid and efficient classification algorithms.

SED-based classification methods typically require a broad wavelength coverage. Depending on the classes one wants to classify these might include other bands like X-rays, infrared or radio. However, most survey projects operate within relatively narrow wavelength ranges. For instance, HSC and DES focus on optical bands, the Two Micron All Sky Survey (2MASS; Skrutskie et al. 2006) on near-infrared (NIR) bands, and the Wide-Field Infrared Survey Explorer (WISE; Wright et al. 2010) on mid-infrared bands. Classifying on the basis of photometric data points with short wavelength intervals may be affected by degeneracy (Buchs et al. 2019). One approach to address this is to combine multiple survey data (e.g., Ilbert et al. 2009; Fotopoulou et al. 2016; Khramtsov et al. 2021; Salvato et al. 2022; Yang & Shen 2023), but this approach can only be applied to targets with overlapping regions and is limited to the depth of the shallowest survey. Traditional morphology-based classification demands high-quality data where low-surface brightness galaxies may be missed. Additionally, classifications suffer intrinsic degeneracies like compact galaxies and high-redshift QSOs confused as point sources. Combining the SED of celestial objects with their morphological features holds promise in mitigating degeneracies during the classification process and fully exploring the scientific potential of survey data (Sevilla-Noarbe et al. 2018; Khramtsov et al. 2019).

Machine learning (ML) technology, with its outstanding speed and accuracy, has been widely applied in the field of astronomical big data processing (e.g., Dieleman et al. 2015; Bai et al. 2019; Logan & Fotopoulou 2020; Szklenár et al. 2020; Chen 2021; Zhou et al. 2021; Dubois et al. 2022; Li et al. 2022; Xie et al. 2023). Unlike traditional methods relying on physical modeling, ML can directly learn and mine the intrinsic features of celestial objects from vast observational data, sometimes even making new discoveries beyond existing theories. Currently, many ML algorithms have been successfully utilized in astronomical classification tasks. Tech-

niques like Random Forests, extreme gradient boosting (XG-Boost), support vector machines (SVM), and artificial neural networks (ANN) are commonly used for analyzing catalogs of photometric or morphological parameters, while convolutional neural networks (CNN) can directly extract information from images or spectra (Cabayol et al. 2019; Li et al. 2019; Tadaki et al. 2020; Nakazono et al. 2021; Chaini et al. 2023). Although some studies have attempted to feed both SED and morphological information into ML models (Fadely et al. 2012; Khramtsov et al. 2019), most studies still adopt parameterized morphological parameters obtained through traditional methods, which can be affected by noise.

Motivated by the potential to enhance classification performance, we construct a multimodal neural network that combines the flexibility of ANN and CNN to simultaneously extract SED and image features, respectively. We have applied this network to the KiDS DR5 dataset to generate a new Star-QSO-Galaxy catalog. In Section 2, we provide a brief introduction to the data from each survey. Section 3 presents the methodology, detailing the construction and training of the multimodal neural network. The findings are discussed in Section 4, followed by the concluding remarks in Section 5.

2. DATA

The aim of this paper is to provide a Galaxy-QSO-Star catalog for KiDS public Data Release 5 (DR5). Ground-truth labels required for supervised ML come from SDSS DR17. Additionally, we adopt Gaia (Gaia Collaboration et al. 2016) DR3 and Galaxy and Mass Assembly (GAMA; Driver et al. 2011) DR4 to further test the performance of classification algorithm to Galactic (stars) and extragalactic (QSOs and galaxies) objects, respectively.

2.1. KiDS

KiDS is a *ugri*-band wide-field imaging survey with the OmegaCAM camera mounted at the VLT Survey Telescope (Capaccioli & Schipani 2011; Capaccioli et al. 2012). The complete observations cover ~ 1350 deg² in the Galactic North and South. 1006 deg² of them have been released under DR4 (Kuijken et al. 2019), while the remaining DR5 is internal data. Thanks to the excellent observing conditions, the *r*-band limiting magnitude is ~ 25 (5σ in 2 square arcsec) with typical seeing of $\sim 0.7''$. In addition, VISTA Kilo-degree Infrared Galaxy (VIKING; Edge et al. 2013) is KiDS partner survey carried out with the VISTA telescope which can complement its near-infrared data in *ZYHJK_s*-band. Therefore, we can obtain a total of 9-band optical-NIR data to separate QSOs from stars and galaxies.

For each object, KiDS DR5 provides its 9-band Gaussian Aperture and PSF (GAAP; Kuijken et al. 2015) magnitudes, and then 8 adjacent band colors (e.g., $u - g$, $g - r$, etc.) can be derived. The GAAP technique is specifically designed to improve color measurement accuracy by homogenizing the PSF across different filters. This is especially important for galaxies and some nearby QSOs. To avoid any confusion introduced by the unreliable measurements, we only adopt the 65,909,027 objects which have all 9-band measurements.

Figure 1 shows the distribution of their *r*-band GAAP magnitude and corresponding $u - g$ color. Considering that supervised machine learning algorithms are limited by the feature space coverage of training samples (see Figure 1), we further select the 27,334,751 objects with $r \leq 23$ mag as inference data (see Section 4). In principle, the reliability of the magnitude measurement should be characterized by the error or the signal-to-noise ratio (S/N), but this can be ignored for bright sources.

2.2. SDSS

DR17 is the final annual release of SDSS-IV (Abdurro'uf et al. 2022) which has cumulated 5,801,200 spectroscopically identified objects in specObj-dr17¹ data base. We apply TOPCAT tool (Taylor 2005) to cross-match SDSS sample with KiDS, and 177,843 objects are obtained within a matching radius of 1 arcsec. To ensure the reliability of SDSS identification, we only select the confident spectroscopic classification measurements depending on the ZWARNING flag (ZWARNING = 0; Bolton et al. 2012), which yield 167,009 objects. The final cross-matched sample includes 31,306 stars, 19,608 QSOs, and 116,095 galaxies. We then randomly split a subset of 127,009 as the training dataset to train the multimodal neural network model described in Section 3, while the remaining 40,000 sources are equally divided into validation and testing datasets. Note that the inference data are deeper than the labeled sample (see Figure 1), thus it is necessary to test the performance of our algorithm.

2.3. Gaia

Gaia is an European Space Agency's all-sky space-astrometry mission launched on 19 December 2013. Its primary science goal is to study the structure and dynamics of the Galaxy through high precision astrometry, which can help us to isolate a clean sample of star with significant parallax or proper motion. There are 1,811,709,771 sources brighter than $G = 21$ (corresponding to $r \approx 20$) in the Gaia DR3 catalog (Gaia Collaboration et al. 2021, 2022), and 4,840,178 of them can be matched to KiDS within 1 arcsec through the CDS Upload X-Match Window of TOPCAT. Then, the most confident stars are selected by the significance of parallax and proper motion. We required that a star in the sample should satisfy either of the following criteria (see also in Yang & Shen 2023):

$$\frac{|\varpi|}{\sigma_\varpi} \geq 5, \quad (1)$$

or

$$\frac{\mu_\alpha^2 + \mu_\delta^2}{\sqrt{\mu_\alpha^2 \sigma_{\mu_\alpha}^2 + \mu_\delta^2 \sigma_{\mu_\delta}^2}} \geq 5, \quad (2)$$

where ϖ , σ_ϖ , μ_α , σ_{μ_α} , μ_δ , and σ_{μ_δ} are parallax, parallax error, proper motion in RA, proper motion error in RA, proper motion in DEC, and proper motion error in DEC, respectively. This selection step results in a sample of 3,444,939.

¹ https://data.sdss.org/datamodel/files/SPECTRO_REDUX/specObj.html

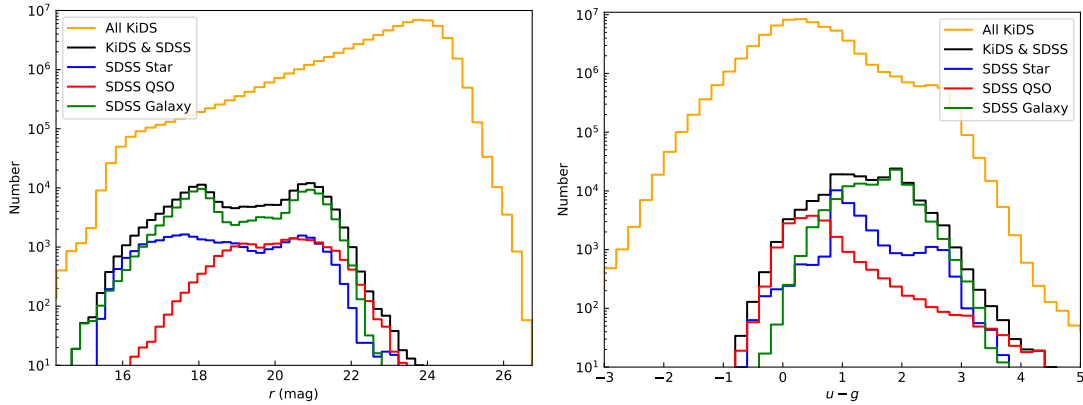


Figure 1. The distributions of r -band magnitude (left panel) and $u - g$ color (right panel) for KiDS and SDSS datasets. In both panels, the black histograms represent the overlapping sources between KiDS and SDSS, the orange histograms depict the data from the KiDS survey, while the blue, red, and green histograms denote stars, QSOs, and galaxies identified by SDSS spectroscopy, respectively.

The final Gaia star dataset contains 3,422,113 sources after removing 22,826 SDSS objects.

2.4. GAMA

GAMA is a spectroscopic survey carried out on the 3.9-m Anglo-Australian Telescope which is designed to study the formation and evolution of cosmology and galaxy. The final data release of GAMA, DR4 (Driver et al. 2022), contains reliable redshift measurements ($NQ > 2$) for 330,542 sources. Most of them are galaxies, while some stars and QSOs can be distinguished by redshift (e.g., the objects with redshifts $z \sim 0$ and $z > 1$ are most likely to be stars and QSOs, respectively). We cross-matched KiDS with GAMA using a radius of 1 arcsec, yielding a sample of 279,404. However, 48,902 of them are duplicated with SDSS observations which may cause bias in the test results. To maintain an independent GAMA sample, we removed these objects, leaving a total of 230,502 sources.

3. METHOD

We employed two standard models, ANN and CNN, both of which are categories of deep learning and significant branches of ML (Smith & Geach 2023). These models are designed based on the concept of emulating the operations of biological neural networks, which in turn allow for the efficient processing and analysis of complex data. ANN (McCulloch et al. 1943), also referred to as Multi-Layer Perceptron (MLP), comprises multiple interconnected layers of artificial neurons that mimic the connections and synaptic processing of biological brains. Each neuron learns weighting and bias parameters to capture nonlinear relationships within inputs, thus enabling accurate prediction and classification. CNN (Lecun et al. 1998), on the other hand, is a specialized neural network architecture that is particularly effective in image and signal processing tasks. By employing components such as convolutional layers, pooling layers, and fully connected layers, CNN is capable of extracting spatial and morphological features from input data. It accomplishes this through weight sharing and local perception mechanisms. As

a result, CNN exhibits superior performance in tasks like image classification and object detection, where its ability to analyze complex visual information is particularly advantageous.

3.1. Neural network architecture

As illustrated in Figure 2, our multimodal neural network integrates two simultaneous branches tailored for feature extraction from SED and image data. These branches aim to capture different attributes of the data: the ANN is tasked with analyzing complex nonlinear patterns in multi-band photometric information, while the CNN focuses on extracting spatial structures and morphological features from astronomical images. The high-level features extracted from both data streams are combined to form a complementary feature vector that feeds into the final classification layers, thereby improving the overall accuracy of our model.

The ANN branch begins with an input layer, where it receives photometric information spanning nine bands along with eight colors derived from adjacent bands. Following this are four fully connected layers, each harboring 512 neurons. These dense layers are dedicated to capturing the complex non-linear relationships embedded within the SED data. The output from the final dense layer is subsequently flattened into a one-dimensional vector containing 8704 elements.

In parallel, the CNN branch operates on a 41×41 pixels ($8' \times 8'$) r -band image input, initiating the feature extraction with a 5×5 convolutional layer comprising 32 channels. This layer is primarily responsible for capturing basic visual features from the image data. This is followed by an average pooling layer, which halves the size of the feature maps while preserving the most critical information. To facilitate deeper learning and more robust feature detection, we incorporate five ResNet (He et al. 2015) basic blocks in succession. These blocks are arranged to address the vanishing or exploding gradient issues by implementing shortcut connections after every two convolutional layers. Each basic block is comprised of four convolutional layers with 3×3 kernels, with the number of filters doubling at each subse-

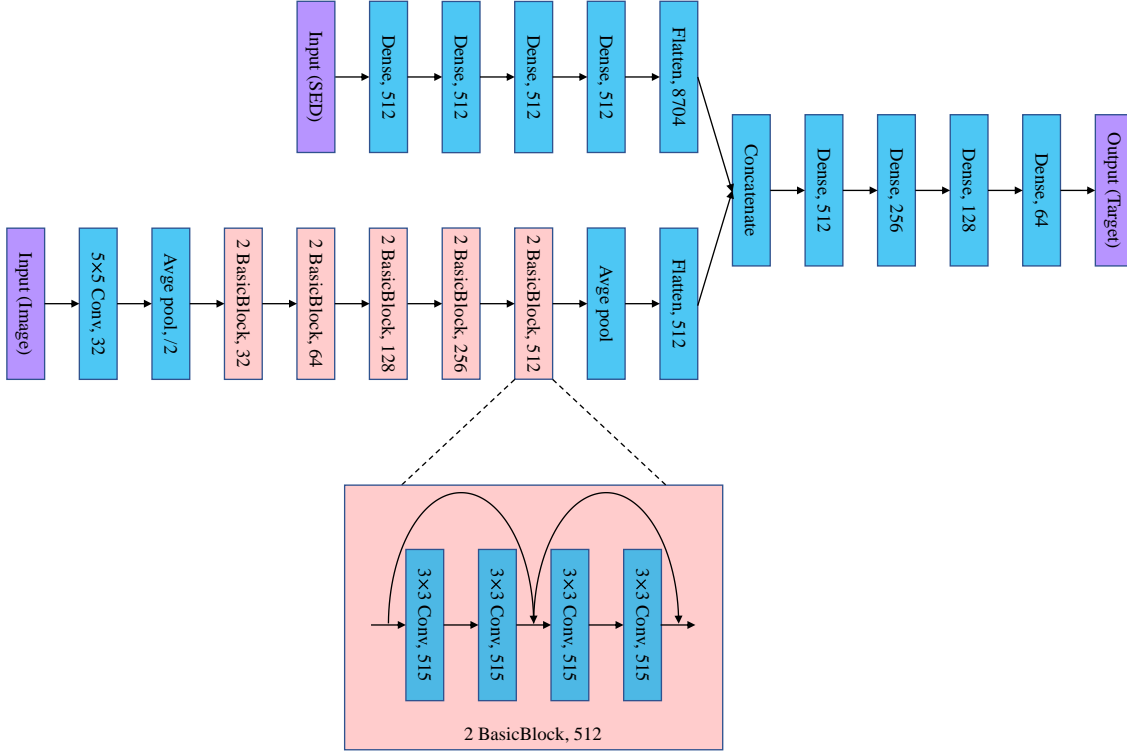


Figure 2. Schematic of the multimodal neural network architecture, consisting of 18,257,155 neurons. Each blue or purple rectangle represents a layer, and each light pink rectangle represents two identical ResNet blocks. The SED branch inputs photometry from 9 KiDS bands and 8 adjacent band colors, and the image branch processes a 41×41 pixels r -band image. The output layer provides classification probabilities for stars, quasars, or galaxies.

quent block—beginning with 32 and incrementing through 64, 128, 256, to 512. The final average pooling layer further compresses the feature dimensions by half, then passing it to a flattening layer that forms another one-dimensional 512-feature vector.

The feature vectors from the ANN and CNN—8704 and 512 dimensions, respectively—are concatenated to form a comprehensive 9216-dimensional vector that incorporates both the photometric and morphological characteristics of the astronomical sources. This integrated vector is then refined through a series of dense layers with a descending number of neurons (512, 256, 128, and 64), progressively reducing the dimensionality of the feature space and concentrating on the most salient features. Culminating the network is a final dense layer with three neurons, corresponding to the categories of stars, galaxies, and QSOs. This output layer employs a softmax activation function to produce a probabilistic distribution over the three classes, facilitating the determination of the most likely category for each astronomical source.

Throughout the network, each hidden layer applies the ReLU activation function to ensure non-linearity and prevent gradient saturation, which is vital for maintaining gradient flow during the training process. We adopted the categorical cross-entropy as our loss function and utilized the Adam optimizer to refine the training of our model.

3.2. Evaluation metrics

In ML, several standard metrics are commonly employed to assess classification performance, including Accuracy, Precision, Recall, and F1-score. These metrics are defined in the following manner:

$$\text{Accuracy} = \frac{\text{TP} + \text{TN}}{\text{TP} + \text{TN} + \text{FP} + \text{FN}}, \quad (3)$$

$$\text{Precision} = \frac{\text{TP}}{\text{TP} + \text{FP}}, \quad (4)$$

$$\text{Recall} = \frac{\text{TP}}{\text{TP} + \text{FN}}, \quad (5)$$

$$\text{F1 - score} = 2 \times \frac{\text{Precision} \times \text{Recall}}{\text{Precision} + \text{Recall}}, \quad (6)$$

where TP (True Positives) is the number of positive samples correctly classified; TN (True Negatives) is the number of negative samples correctly classified; FP (False Positives) is the number of negative samples misclassified as positive; FN (False Negatives) is the number of positive samples misclassified as negative.

Accuracy, as shown in Equation 3.2, reflects the proportion of all correctly classified samples and provides a direct metric for evaluating overall model performance. However, this indicator may be ineffective in the case of imbalanced

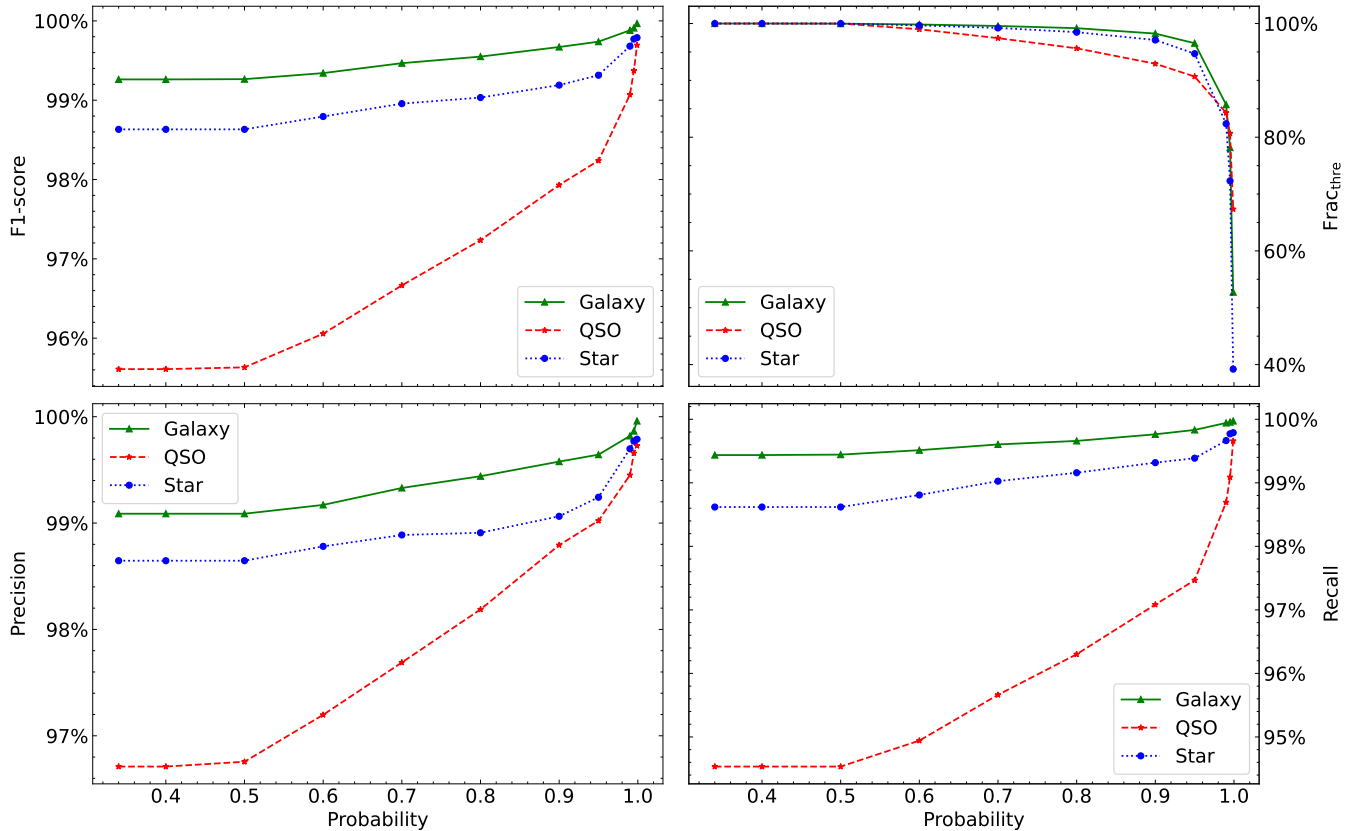


Figure 3. Evaluation metrics for classification of stars, quasars, and galaxies at different output probability thresholds. The panels display F1-score (top left), $\text{Frac}_{\text{thre}}$ (top right), Precision (bottom left), and Recall (bottom right), with blue, red, and green lines representing the metrics for stars, quasars, and galaxies, respectively.

datasets. Consequently, it is primarily utilized to search for the optimal model on the validation dataset, rather than to evaluate the detailed performance of each class.

Precision, also known as Purity in astronomy, quantifies the fraction of true positives among the predicted positives. Recall represents the proportion of all positive samples that are successfully identified by the model, equivalent to Completeness in astronomy. It is important to note that ML practitioners often enhance classification confidence by setting a threshold for output probabilities, potentially excluding data below the threshold. When calculating Recall, some studies count these below-threshold samples as FN, while others completely ignore them. In scenarios where they are included, Recall still aligns with Completeness, otherwise, Recall needs to be adjusted by multiplying the fraction of samples above the threshold ($\text{Frac}_{\text{thre}}$). Therefore, in our analysis of the testing dataset, we compute $\text{Frac}_{\text{thre}}$ for different thresholds. The F1-score, the harmonic average of Precision and Recall, is particularly valuable as it provides a balanced measure of classification performance, reflecting the overall efficacy of the model across each category of sources. This metric was instrumental in evaluating the ability of our multimodal neural network to classify astronomical sources. Figure 3 displays the distribution of these evaluation met-

rics across different output probability thresholds, with corresponding values tabulated in Table 1.

Additionally, the confusion matrix is a powerful tool for evaluating classification problems, offering a visual representation of the relationship between model predictions for each class and the actual ground-truth categories. Figure 4 illustrates the results at an output probability threshold of 0.995, where each column represents the number of predictions for the corresponding class, and each row represents the ground-truth classes. To render the classification precision of each category more discernible, we have normalized the confusion matrix and displayed it in a percentage format.

3.3. Implementation

Our neural network model is implemented and trained using Keras², a high-level open-source API that provides a user-friendly interface built on top of the TensorFlow³ framework. For the training and testing process, we utilized a GPU-accelerated computer equipped with NVIDIA GeForce RTX 3080 laptop GPU to enhance computational efficiency.

² <https://keras.io>

³ <https://www.tensorflow.org>

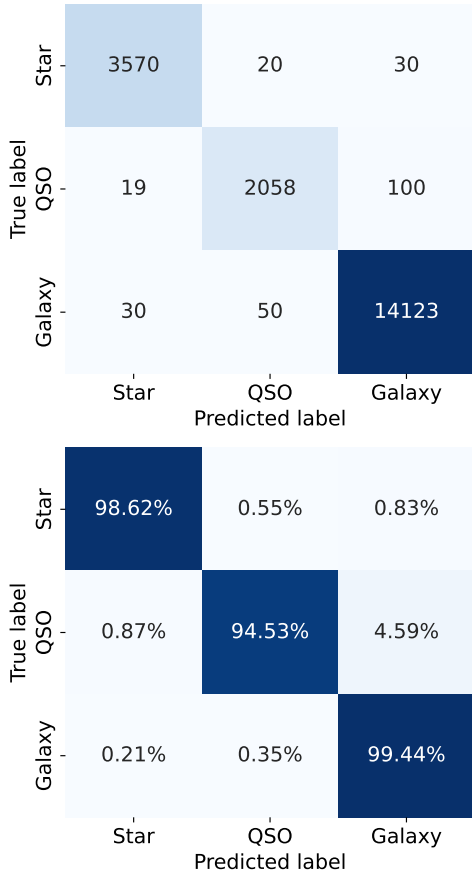


Figure 4. Confusion matrix for the internal testing dataset. Each panel has predicted categories (star, quasar, galaxy) on the vertical axis and true categories from SDSS on the horizontal axis. The top panel shows the number of targets predicted in each category, while the bottom panel shows these numbers normalized as percentages.

During the training phase, the hyperparameters such as batch size and regularization factor were determined through repeated experiments. We found that setting the batch size and regularization factor to 128 and 0.001, respectively, was sufficient to achieve good performance on the testing dataset (containing 20,000 samples). To rapidly and accurately pinpoint the optimal model, we employed a tiered learning rate strategy, conducting training at learning rates of $1e-3$, $1e-4$, and $1e-5$, across 30 epochs for each rate. Each epoch took approximately 34 seconds, with a total training time of ~ 51 minutes. We then selected the best model based on the minimum loss and maximum accuracy on the validation dataset. This model achieved nearly identical performance on the testing dataset, and we arbitrarily chose the model with the lowest loss to make predictions on the full dataset.

4. RESULTS AND DISCUSSION

We assessed the overall classification capability and applicability of the proposed multimodal neural network by examining its performance on an independent internal testing dataset. Furthermore, two external datasets were utilized

Table 1. Classification Performance at Different Thresholds.

Threshold	Class	Precision (%)	Recall (%)	F1-score (%)	Frac _{thre} (%)	Completeness (%)
$p \geq p_{\max}$	Star	98.65	98.62	98.63	100.00	98.62
	QSO	96.71	94.53	95.61	100.00	94.53
	Galaxy	99.09	99.44	99.26	100.00	99.44
$p \geq 0.5$	Star	98.65	98.62	98.63	100.00	98.62
	QSO	96.76	94.53	95.63	100.00	94.53
	Galaxy	99.09	99.44	99.27	99.98	99.42
$p \geq 0.8$	Star	98.91	99.16	99.03	98.48	97.65
	QSO	98.19	96.30	97.24	95.64	92.10
	Galaxy	99.44	99.66	99.55	99.18	98.85
$p \geq 0.9$	Star	99.06	99.32	99.19	97.10	96.44
	QSO	98.79	97.08	97.93	92.93	90.22
	Galaxy	99.58	99.76	99.67	98.23	98.00
$p \geq 0.99$	Star	99.70	99.66	99.68	82.38	82.10
	QSO	99.45	98.69	99.07	84.29	83.19
	Galaxy	99.82	99.94	99.88	85.74	85.69
$p \geq 0.995$	Star	99.77	99.77	99.77	72.32	72.15
	QSO	99.66	99.09	99.37	80.66	79.93
	Galaxy	99.87	99.95	99.91	78.19	78.15
$p \geq 0.999$	Star	99.79	99.79	99.79	39.23	39.14
	QSO	99.73	99.66	99.69	67.34	67.11
	Galaxy	99.96	99.97	99.97	52.74	52.73

NOTE—Evaluation metrics including Precision, Recall, F1-score, Frac_{thre}, and Completeness at different output probability thresholds for stars, quasars, and galaxies.

to validate the robustness and generalization ability of the model beyond the training sample space. Finally, we applied the trained network to the full KiDS DR5 dataset and generated a new Star-QSO-Galaxy catalog for objects brighter than 23 mag in r -band.

4.1. Performance on Testing Datasets

4.1.1. Internal Testing Dataset

Although the validation dataset was not directly involved in model training, its role in model selection may inadvertently lead to overfitting, thereby increasing the risk of information leakage. To address this concern and objectively assess the performance of our model, we randomly selected 20,000 spectroscopically confirmed sources from the SDSS-KiDS cross-matched sample to compose an independent testing dataset. The sample was exclusively for final testing, without participating in the training or validation stages. This ensures an unbiased assessment, mitigating the potential for the model to overfit to any particular subset of the data.

On this isolated testing dataset, our multimodal neural network achieved an overall accuracy of 98.76%, closely aligning with the 98.69% accuracy observed in the validation dataset. Such consistency indicates that our model generalizes well from the validation phase to unseen new data, which is crucial for practical applications. We then conducted more detailed performance assessments on each class of sources, including Precision, Recall, and F1-score. The results are presented in Figure 3 and Table 1.

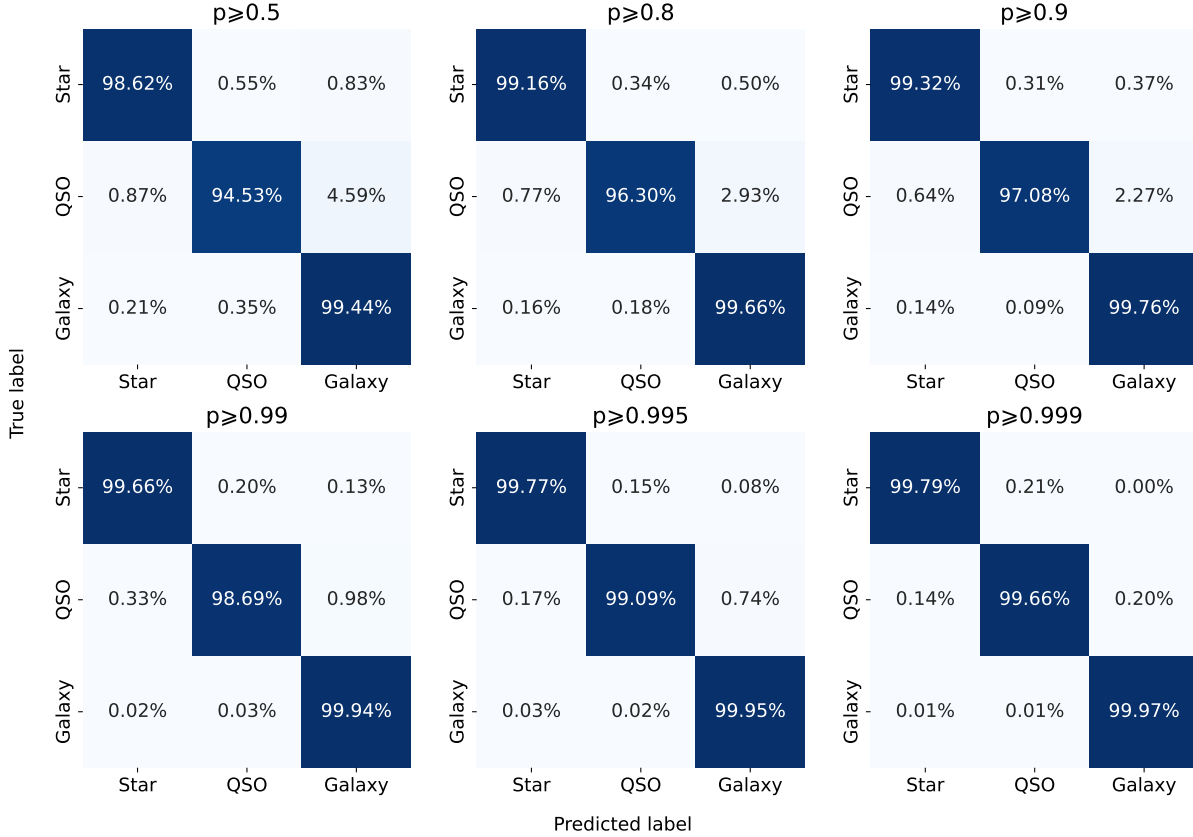


Figure 5. Same as Figure 4 but for confusion matrices at different output probability thresholds, showing how the predictive performance changes with the adjustment of the threshold.

The classification metrics revealed that galaxies exhibited the best performance with all three metrics exceeding 99%. This success is largely attributed to the enormous galaxy sample size used during training. This was followed by the stars, with all metrics also exceeding 98.6%, reflecting robust identification of these two types of celestial objects. QSOs achieved slightly lower Precision and Recall at 96.71% and 94.53% respectively, likely due to the relatively smaller training sample size, as well as the potential for misclassification of some low-redshift active galactic nuclei as galaxies due to contamination from their host galaxies. This latter point is evidenced by the confusion matrix depicted in Figure 4, where the majority of misclassified QSOs were grouped with galaxies. Despite this, a robust F1-score of 95.6% demonstrates that the model is still reliable in terms of QSO classification.

In machine learning paradigms, our model assigns a probability vector to each target for classification, with each value representing the likelihood of a predefined class (such as Stars, QSOs, or Galaxies in our definition). The sum of these probabilities is 1, and typically, a higher probability (p) for a target being classified into a certain class indicates greater confidence, which implies higher Purity (Precision). Therefore, we can set a threshold for p , retaining only those samples that exceed this threshold as the final result, thereby enhancing the sample Purity. It is important to note that this

strategy, while beneficial for sample Purity, may decrease the Completeness of the sample. For example, a higher threshold may exclude objects with insufficient classification confidence, potentially leading to the absence of some actual category members in the final catalog.

To balance Purity and Completeness in various astronomical applications, we tested the performance of our multimodal neural network at different thresholds. Figure 3 shows the variations in evaluation metrics as a function of the threshold, with some detailed values listed in Table 1. As expected, an increase in the threshold can improve Precision, Recall, and the F1-score, whereas $\text{Frac}_{\text{thre}}$ and the derived Completeness ($\text{Frac}_{\text{thre}} \times \text{Recall}$, as shown in Table 1) exhibit a declining trend. We also examined the confusion matrix at different thresholds (Figure 5), and the results showed a clear decrement in misclassification rates with threshold increments. This trend suggests that raising the threshold for p indeed amplifies the Purity of the sample but at the cost of Completeness.

An analysis of Figures 3 and 5 reveals that the choice of probability threshold significantly impacts the classification of QSOs, in contrast to a minor effect on the classification of Galaxies. This is primarily because the model already achieves excellent performance in predicting Galaxies, leaving limited scope for further refinement. Intriguingly, we found that when the threshold is fixed at 0.9, the Complete-

ness for all categories can be maintained above 90%, and the Purity exceeds 98%. As the threshold is further increased to 0.99, Purity can reach above 99%, while Completeness still maintains a level of 82%. Beyond this point, Completeness quickly declines despite a marginal gain in Purity. Hence, setting the probability threshold between 0.9 to 0.99 appears to offer an effective balance between Purity and Completeness.

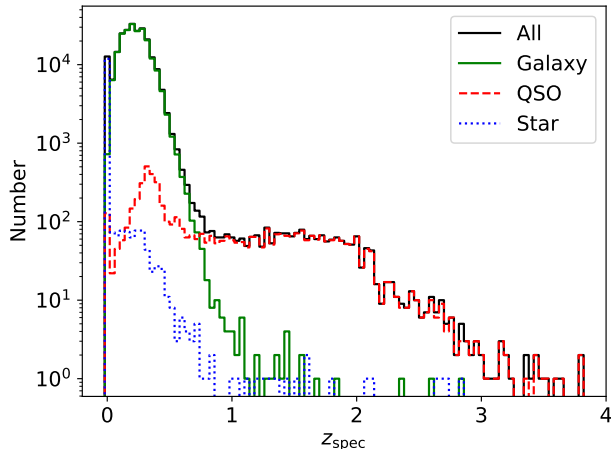


Figure 6. Redshift distribution for the GAMA testing dataset. The black solid line shows the distribution for all targets, while the blue dotted line, red dashed line, and green solid line represent the distributions for targets predicted as stars, quasars, and galaxies by the multimodal neural network, respectively.

4.1.2. External Testing Datasets

Considering the issue of pre-selected sources in the SDSS dataset, there is potential for our neural network model to overfit to this data. To comprehensively evaluate the generalization capability of the model in practical applications, it is necessary to validate it on external datasets. Currently, most publicly released spectroscopic survey data have limited overlap with KiDS, which constrains the availability of extensive testing samples. We primarily utilize Gaia and GAMA as external data sources to verify the generalization performance of our model on stellar and galaxy (including QSO) classification, respectively.

Most targets in the Gaia database do not have corresponding spectroscopic observations, but its high-precision astrometric measurements enable us to filter out a pure stellar sample. This sample is considered unbiased in terms of stellar radiation and can effectively avoid potential selection effects. Through cross-matching with KiDS, we obtained over 3.4 million independent testing samples (see Section 2.3). None of these data were involved in model tuning or evaluation. The test results showed that as high as 99.74% of the targets were correctly predicted as stars, even exceeding the performance on the internal testing dataset. This discrepancy is mainly attributed to the contamination present in SDSS

spectroscopic classifications (see Section 4.2), indicating that our algorithm actually has superior performance in star classification.

For extragalactic objects, we adopted the abundant spectroscopic redshift galaxy sample from GAMA for testing. Over 230k of these targets that overlap with KiDS but not with SDSS. The prediction results revealed that only 97.70% of the targets were categorized as galaxies, with the remaining 1.21% classified as stars and 1.11% as quasars, which did not appear to meet expectations. However, upon further examination of the redshift distribution of these targets (see Figure 6), we found that the majority of those predicted as stars had redshifts around 0, confirming that they indeed reside within the Milky Way. After removing these low-redshift (arbitrarily chosen $z < 0.04$) targets, the fraction of categorized as galaxies increased to 98.72%, while stars and quasars accounted for 0.26% and 1.02%, respectively. Figure 6 also shows that targets with redshifts greater than 0.8 were almost all classified as QSOs. Given the depth of the GAMA survey, it is unlikely to observe such high-redshift galaxies, so these classification results should be reasonable. If QSO classification is also regarded as correct, we can conclude that the classification Precision for extragalactic objects reached 99.74%.

In this test, we did not impose any restrictions on the threshold of p , but the model still demonstrated excellent performance for both Galactic and extragalactic targets, further confirming the stability and reliability of our algorithm across different datasets. This establishes a solid foundation for future applications to more extensive samples and other survey data.

4.2. Limitations and Challenges

In addition to the choice of ML algorithms, data quality fundamentally determines the upper limit of model performance. Clean data allows the model to focus on learning the underlying patterns that are consistent with the real-world problems during the training process, thereby enhancing its stability and interpretability. Conversely, dirty data may mislead the learning process of model parameters and evaluation results, increasing the risk of overfitting. Indeed, there are some misclassified targets in the SDSS spectral data (Bolton et al. 2012; Lyke et al. 2020). However, since the proportion of these misclassifications is relatively low (about only a few percent), the model still performs impressively well on the testing dataset. This can also be attributed to the strong noise-resistant capability of DNNs, as well as the use of techniques such as regularization and batch training during the training process. Through random inspection of misclassified samples, we found that some SDSS labels themselves were erroneous, and our multimodal neural network model was even able to effectively correct these errors, especially for galaxies misclassified as stars by SDSS (as shown in Figure 7).

The performance of the model is also influenced by the data volume. A larger dataset can provide richer and more detailed feature representations, which helps the model learn complex patterns and effectively mitigate noise and outlier. This, in turn, enhances its accuracy and generalization abil-

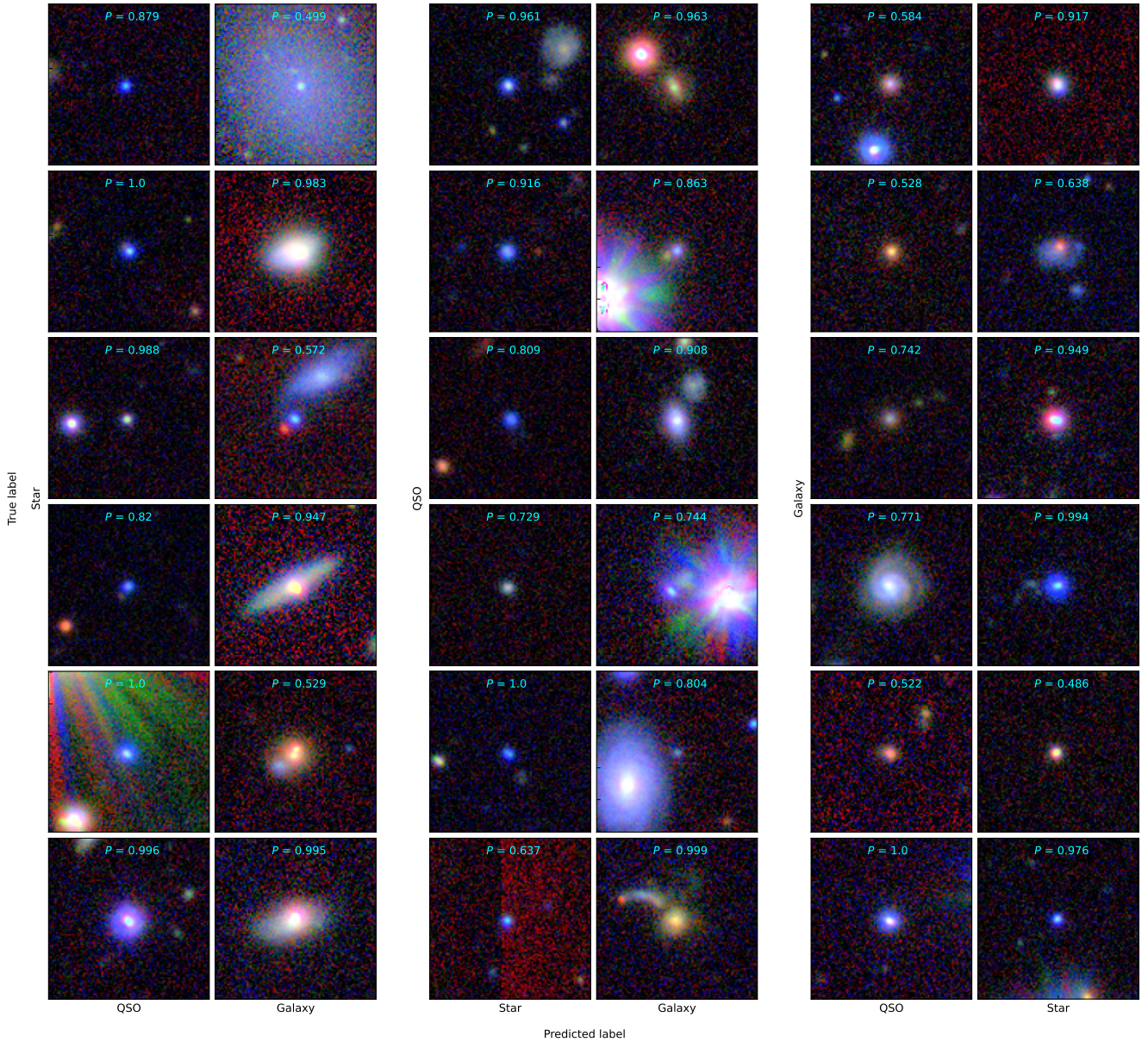


Figure 7. *gri* color-composed images of some misclassified targets. The vertical axis represents the spectral classification labels from SDSS, and the horizontal axis represents the predictions made by the multimodal neural network.

ity. In our training, the number of quasar samples was significantly less than that of stars and galaxies, which somewhat limited the recognition capabilities of the model for these targets. This indicates that although our method has demonstrated impressive classification performance, there is still room for further improvement as spectral data continues to accumulate in the future.

Due to the inherent extrapolation uncertainty of ML models, their applicability typically depends on the coverage of the feature space by the known data. In our study, the SDSS spectroscopic depth in the *r*-band is approximately 22 mag, which is ~ 2 mag brighter than KiDS, and there are also differences in the color distribution between them (see Figure 1). Therefore, it is necessary to filter the prediction data

to ensure the reliability of the final results. This requires understanding the specific feature space boundaries of the model, which is a challenge for neural network models. We primarily compared the brightness and color distributions of the two databases—historically the most commonly used features—and found that the most significant difference was in brightness. By limiting our focus to targets with *r*-band magnitudes brighter than 23, we found that the color distribution of most KiDS data aligned with SDSS (e.g., 99.96% of *u* – *g* colors were within the range of -1 to 4). This phenomenon may be related to the requirements in the data preprocessing stage, where all bands must have reliable photometric detection values, thus excluding some extremely red and blue targets. The color consistency increases our confidence in

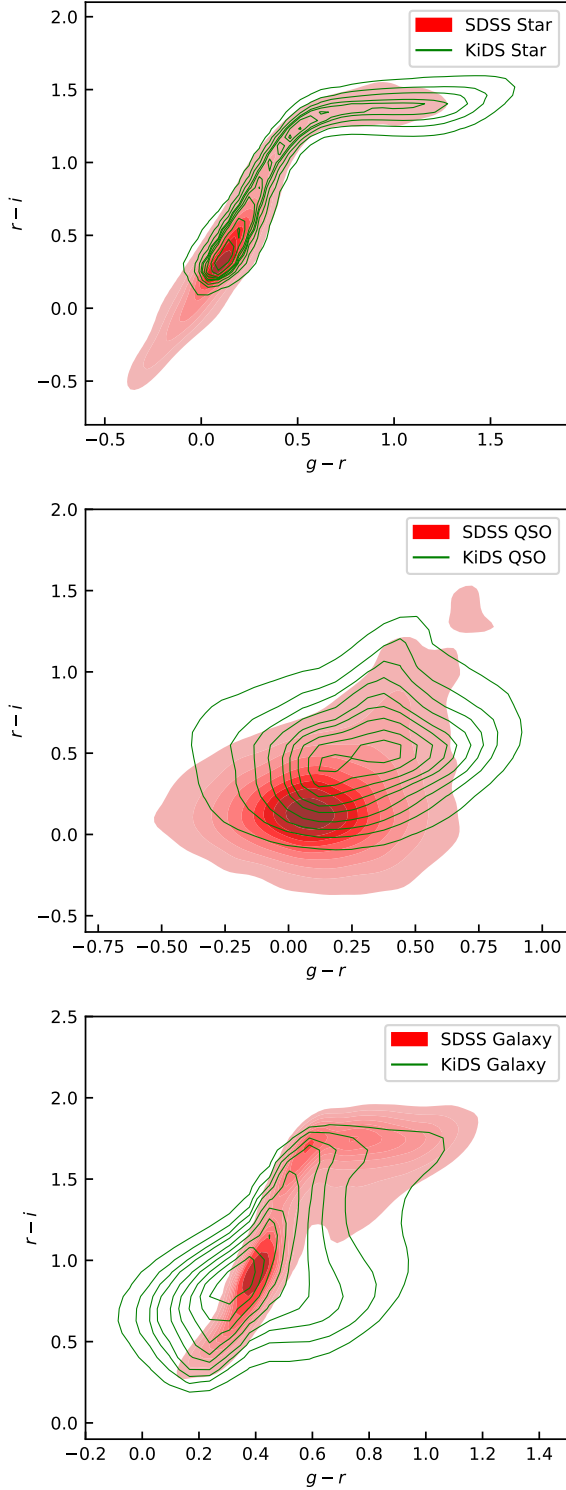


Figure 8. Color-color diagrams ($g-r$ vs. $r-i$) for KiDS and SDSS datasets. From top to bottom, the panels represent stars, QSOs, and galaxies. The red shaded regions indicate the cross-matched data between SDSS and KiDS, while the blue contours represent all KiDS data brighter than 23 mag.

the prediction results for brighter sources, but also introduces limitations for the model in identifying targets with extreme color properties.

To determine the applicable brightness range of the model, we conducted the following tests. First, we selected two equal-sized samples based on their r -band magnitudes, with brightness ranges of $16.5 \leq r < 18.5$ mag and $18.5 \leq r < 20.5$ mag, respectively. By comparing the model performance of these two brightness groups, we found that their classification abilities were basically equivalent. Even when extrapolating the testing data by 1 mag toward the faint end, the performance evaluation metrics did not show a significant decline for either model. Subsequently, we further tested the model using three different brightness thresholds ($r < 19$ mag, $r < 20$ mag, and $r < 21$ mag), confirming that all three results could essentially extrapolate by 1 mag under these conditions. These two tests help us infer that our multimodal neural network can effectively handle targets with magnitudes up to ~ 23 mag.

While there may be other feature restrictions besides brightness, the testing results from the Gaia and GAMA surveys suggest that their impact is not substantial. These two datasets, apart from the targets being relatively bright ($r < 20$ mag), may have different feature distributions compared to SDSS, but our model still performs very well on them, indicating that within the permissible brightness range, the model can be well generalized to new data.

Furthermore, some intrinsic issues with KiDS data could also affect the accuracy of the final predictions. For instance, the presence of obvious companions or saturation around some targets (as shown in Figure 7) may impact the measurement of target flux or the extraction of morphological features, potentially leading to misclassification. Systematically addressing these issues requires comprehensive cleaning and preprocessing of predictive data, which is beyond the scope of this study.

4.3. Application to KiDS DR5

We apply the trained multimodal neural network model to the entire KiDS DR5 dataset to predict the categories of target sources. Our goal is to compile a new Star-QSO-Galaxy catalog covering an area of approximately 1350 deg^2 . According to our prior testing outcomes, we only classify targets with an r -band magnitude less than 23. To facilitate diverse research interests, we provide the r -band magnitude and the associated maximum output probability (p_{\max}) for each target, with detailed information listed in Table 2.

This value-added catalog contains a total of 27,334,751 targets, of which 6,427,859 are identified as stars, 3,304,636 as quasars, and 17,602,220 as galaxies. Notably, 13,068,232 targets fall within the $22 < r \leq 23$ mag range in the r -band, which are extrapolated results, accounting for nearly half ($\sim 47.81\%$) of the total number of targets. This portion of the data exceeds the brightness range directly trained by our model, yet the model has demonstrated acceptable ac-

Table 2. Column Descriptions of the KiDS DR5 Galaxy-QSO-Star Catalog

No.	Column Name	Description	Units	Datatype
1	Name	KiDS unique source identifier from ASTRO _{band} table	-	string
2	RA	J2000 Right Ascension	degree	double
3	DEC	J2000 Declination	degree	double
4	r	KiDS r -band GAAP magnitude	mag	double
5	class	classification: STAR/QSO/GALAXY	-	string
6	p_{\max}	Maximum output probability	-	double

NOTE—Description of columns in the KiDS DR5 Galaxy-QSO-Star Catalog. The table lists the properties stored for each object, including identifiers, coordinates, magnitudes, classification results, and probabilities.

curacy and stability within this magnitude range in previous tests. Therefore, we decide to include these extrapolated results in the final catalog.

To validate the effectiveness of our final classification results, we compared the $g - r$ vs. $r - i$ color-color distributions of stars, QSOs, and galaxies in our KiDS catalog with those in the SDSS dataset. As shown in Figure 8, the results exhibit a general agreement between the two datasets, suggesting that our model successfully captures the overall color properties of different sources. Furthermore, we examined the size-magnitude diagram for each class of sources for each class of sources, which is a commonly used method to differentiate between stars and galaxies (e.g., Zuntz et al. 2018). Here, we adopt the half-light radius ($R_{1/2}$) to represent size, and the magnitude is in the r -band. The results are shown in Figure 9. It is evident that stars are primarily located at the brighter end, with sizes typically consistent with the PSF, reflecting their point-source nature. In contrast, galaxies are predominantly found at the fainter end and exhibit significantly larger sizes compared to stars, indicative of their more extended structures. Quasars are primarily distributed between the star and galaxy populations in the size-magnitude space. This distribution aligns well with known observational characteristics and supports our classification results.

Figure 10 presents the r -band magnitude distribution for each category, revealing a dominance of stars at the brighter end ($r < 20$ mag), while the number of quasars and galaxies increases rapidly towards the faint end, which aligns with empirical expectations. Moreover, the distribution of p_{\max} (Figure 10) indicates exceedingly high classification confidence for the majority of targets. Over 85% of the catalog entries have a $p_{\max} \geq 0.9$, and remarkably, for targets with $r \leq 22$ mag, this proportion exceeds 91%. This means that even under relatively stringent selection criteria, we can still obtain about 13 million high-confidence classification results.

4.4. Model Interpretation

Neural network models are often regarded as “black boxes” with internal decision-making processes that are opaque to humans. This opacity makes it difficult to directly analyze the intrinsic connections between celestial object classification and their physical properties. Here, we at-

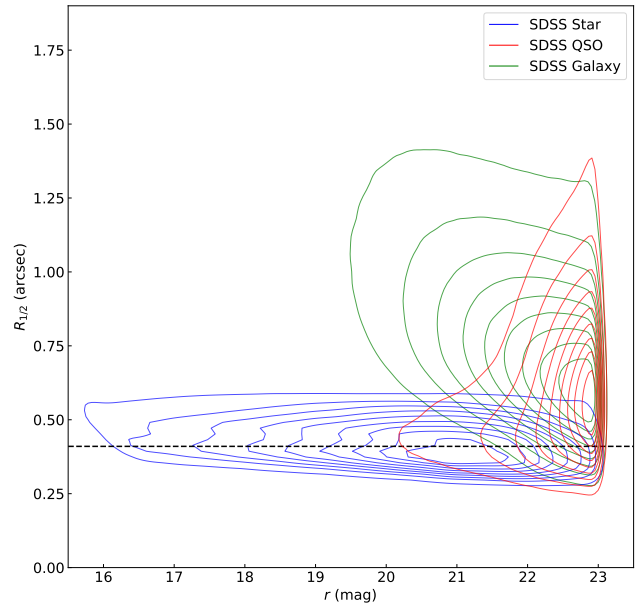


Figure 9. The r vs. $R_{1/2}$ for objects in our catalog. The contours represent the density distribution of stars (blue), QSOs (red), and galaxies (green). The dashed line (black) at $0.41''$ indicates the $R_{1/2}$ corresponding to the average KiDS r -band seeing of $0.7''$, assuming a Gaussian PSF where $R_{1/2} \approx 0.5887 \times \text{FWHM}$.

tempt to use empirical knowledge to explain the features that the model may have learned during its training, aiming to better understand the physical mechanisms behind its excellent performance.

The proposed multimodal neural network extracts information from two input branches: SED and image. As shown in Figure 11, different types of celestial objects inherently exhibit distinct SED and morphological characteristics. The SED primarily reflects the differences in internal radiation mechanisms and the distances (redshifts) of the objects. Stars, for instance, typically exhibit SEDs that can be approximated by blackbody radiation, with peak positions mainly determined by their effective temperatures. On the other hand, the spectrum of quasars in the ultraviolet to optical bands is dominated by the “big blue bump”, a feature produced by high-temperature radiation from the accretion

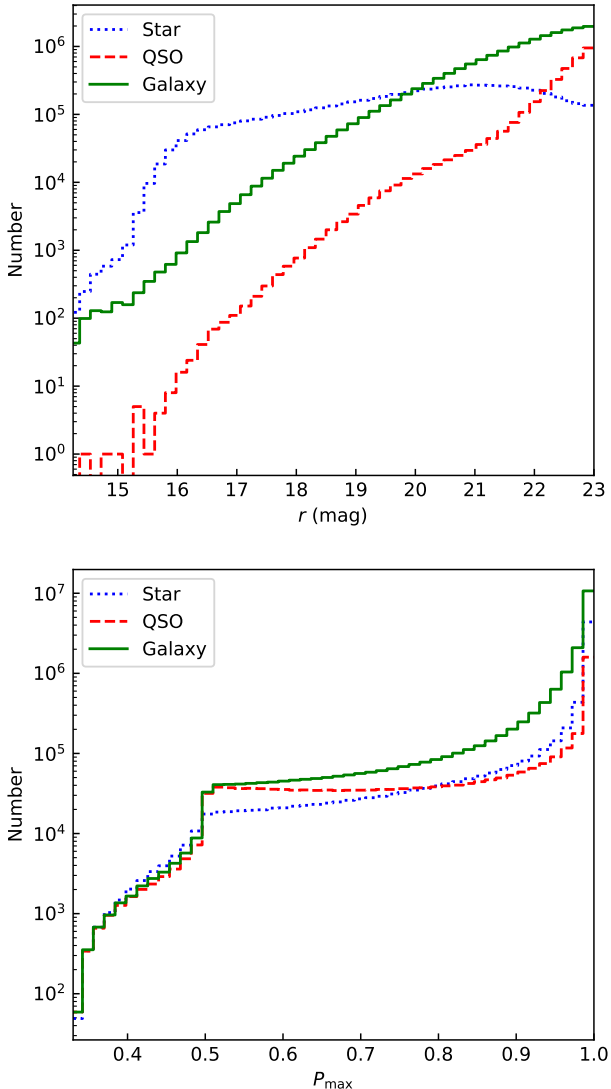


Figure 10. Distribution of r -band magnitude (top panel) and maximum output probability (bottom panel) for each type of object in the value-added catalog. Each panel plots the distribution for targets predicted as stars (blue dotted line), quasars (red dashed line), and galaxies (green solid line).

disk, while the near-infrared is predominantly emission from hot dust (Sanders et al. 1989; Elvis et al. 1994). The multi-wavelength luminosity of galaxies is more complex, as it involves the combined effects of stellar populations and dust (Conroy 2013). The nine-band photometric data provided by KiDS spans a broader wavelength coverage than SDSS spectra, potentially yielding additional physical information. For example, the SED peak of M-type stars is located in the near-infrared band (see Figure 11), and as the redshift increases, the contribution of the “big blue bump” in quasars becomes more pronounced in the optical-near-infrared bands. This prior knowledge suggests that the model may achieve clas-

sification by learning the relative brightness across multiple bands.

For the imaging side, it can provide rich details of the morphology of celestial objects. These morphological features not only contain information about the physical nature of objects but might also refine flux measurements, as the shapes of different objects can affect the results of GAAP measurements. To test the impact of images on classification, we separately used MLP to classify the SED (see Appendix), and found that the performance was significantly inferior to the multimodal neural network. This demonstrates that incorporating morphological information can indeed significantly improve classification efficacy. To further confirm which information directly aids classification, we normalized all images and found that there was a negligible effect on model performance. This implies that during the classification process, the model primarily relies on the physical morphological features rather than simply re-measuring the flux from the images. This is consistent with the human inferential strategies, where we prefer to use the physical properties of morphology itself rather than mere flux correction when classifying. For example, extended galaxies are easily distinguishable from stellar point sources, and the size can be used to estimate the distance of the galaxy (see also Figure 9). For high-redshift quasars and compact galaxies, they may appear more like stars in images, but we can at least rule out the possibility of them being low-redshift extragalactic objects.

In summary, the multimodal neural network can extract luminosity information from photometric data and morphological features from image data, and mapping both to a high-dimensional feature space via a nonlinear function. Within this space, various categories are effectively separated, thus achieving the purpose of classification. The accuracy and efficiency of this method hold promise for widespread application in next-generation multi-color survey projects such as LSST, WFST (Wang et al. 2023), and Mephisto (Han et al. 2022). Future space survey projects (e.g., CSST and Euclid) will provide unprecedented high-resolution images and slitless spectral data, which will further refine our model and enhance the precision of astronomical classification. Moreover, the anticipated wealth of spectral data from future spectroscopic surveys will enable our model to extend its performance to fainter magnitudes.

5. CONCLUSION

In this work, we have developed a multimodal neural network architecture that effectively combines morphological information from images and multi-band photometry for the classification of stars, quasars, and galaxies in the KiDS DR5 survey. By training on SDSS spectroscopic labels and testing on both internal and external datasets, we demonstrate the model’s high accuracy, robustness, and ability to generalize to new data. Our key findings are:

1. On the internal SDSS testing dataset, the model achieves an overall accuracy of 98.76%, with per-class F1 scores of 98.63%, 95.61%, and 99.26% for stars,

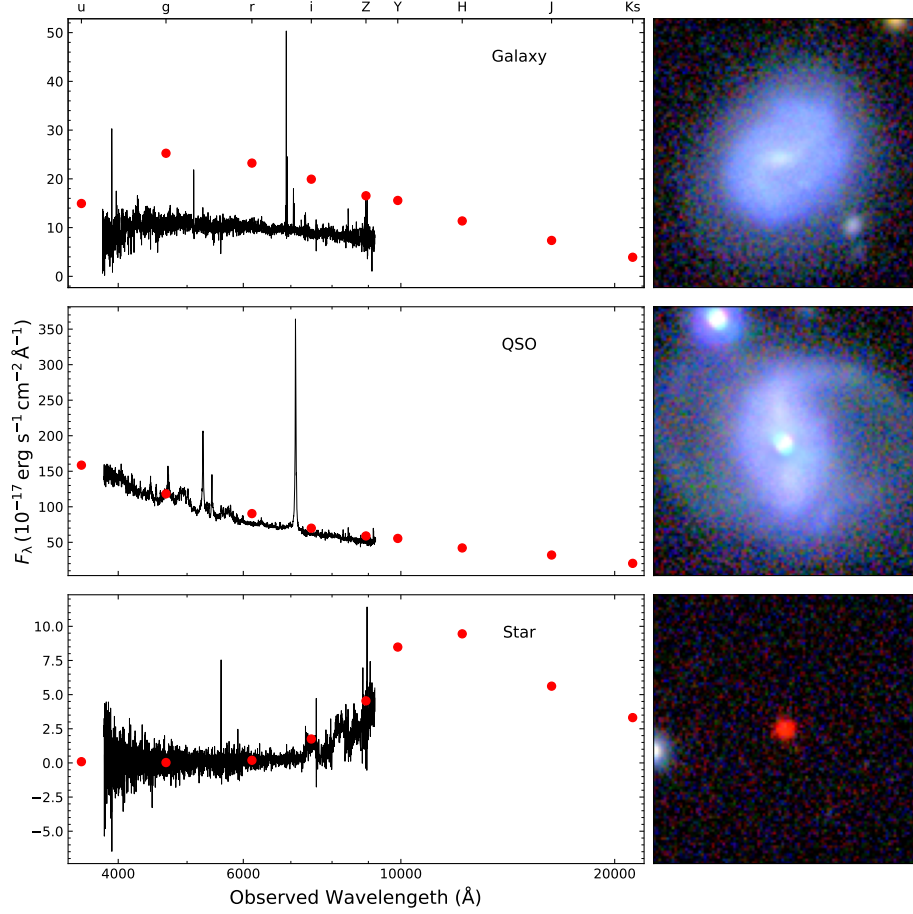


Figure 11. Examples of spectra, SEDs, and images for different categories. The left panels show the SDSS spectra (black solid line) and the SEDs from KiDS nine bands (red points). The right panels show color-composited images from KiDS *gri*-bands.

- QSOs, and galaxies respectively. Raising the output probability threshold can boost purity at the cost of completeness.
2. The model correctly classifies 99.74% of a pure Gaia star sample, higher than the performance on the SDSS testing dataset, indicating potential mislabeling in SDSS that the network helps correct. It also correctly classifies 99.74% of GAMA galaxies after accounting for low-redshift contaminants.
 3. We apply the model to classify over 27 million KiDS DR5 sources down to $r = 23$ mag. Over 85% of the resulting catalog has a maximum probability ≥ 0.9 , indicating high classification confidence.
 4. The model's strong performance stems from its ability to extract both morphological and SED features. Normalizing images has little effect, showing the network relies on physical morphological information rather than just flux correction. Compared to an SED-only MLP, the multimodal network achieves significantly better performance.

This work presents a novel and effective approach for classifying astronomical sources by leveraging deep learning to combine imaging and photometric data. The resulting catalog will enable a wide range of galaxy evolution, large-scale structure, and cosmology studies with KiDS DR5. Future work will extend the technique to a wider range of surveys and wavelengths, and explore its potential for identifying unusual objects. Integrating multimodal information with deep learning offers a promising tool for maximizing the scientific return from the next generation of large-scale astronomical surveys.

This work is supported by National Key R&D Program of China (No. 2021YFA1600404), the National Natural Science Foundation of China (NSFC grants No. 12303022, 12203096, 12203050, 12373018, 11991051, and 12203041), Yunnan Fundamental Research Projects (grants NO. 202301AT070358 and 202301AT070339), Yunnan Postdoctoral Research Foundation Funding Project, Special Research Assistant Funding Project of Chinese Academy of Sciences, and the science research grants from the China Manned Space Project with No. CMS-CSST-2021-A06, NRRN acknowledges financial support from the NSFC, Re-

search Fund for Excellent International Scholars (grant No. 12150710511), and from the research grant from China Manned Space Project n. CMS-CSST-2021-A01.

This research made use of the cross-match service provided by CDS, Strasbourg. Based on data products from observations made with ESO Telescopes at the La Silla Paranal Observatory under programme IDs 177.A-3016, 177.A-3017 and 177.A-3018, and on data products produced by Target/OmegaCEN, INAF-OACN, INAF-OAPD and the KiDS production team, on behalf of the KiDS consortium. OmegaCEN and the KiDS production team acknowledge support by NOVA and NWO-M grants. Members of INAF-OAPD and INAF-OACN also acknowledge the support from the Department of Physics & Astronomy of the University of Padova, and of the Department of Physics of Univ. Federico II (Naples). Funding for the Sloan Digital Sky Survey IV has been provided by the Alfred P. Sloan Foundation, the U.S. Department of Energy Office of Science, and the Participating Institutions. SDSS-IV acknowledges support and resources from the Center for High Performance Computing at the University of Utah. The SDSS website is www.sdss4.org. SDSS-IV is managed by the Astrophysical Research Consortium for the Participating Institutions of the SDSS Collaboration including the Brazilian Participation Group, the Carnegie Institution for Science, Carnegie Mellon University, Center for Astrophysics — Harvard & Smithsonian, the Chilean Participation Group, the French Participation Group, Instituto de Astrofísica de Canarias, The Johns Hopkins University, Kavli Institute for the Physics and Mathematics of the Universe (IPMU) / University of Tokyo, the Korean Participation Group, Lawrence Berkeley National Laboratory, Leibniz Institut für Astrophysik Potsdam (AIP), Max-Planck-Institut für Astronomie (MPIA Heidel-

berg), Max-Planck-Institut für Astrophysik (MPA Garching), Max-Planck-Institut für Extraterrestrische Physik (MPE), National Astronomical Observatories of China, New Mexico State University, New York University, University of Notre Dame, Observatório Nacional / MCTI, The Ohio State University, Pennsylvania State University, Shanghai Astronomical Observatory, United Kingdom Participation Group, Universidad Nacional Autónoma de México, University of Arizona, University of Colorado Boulder, University of Oxford, University of Portsmouth, University of Utah, University of Virginia, University of Washington, University of Wisconsin, Vanderbilt University, and Yale University. This work has made use of data from the European Space Agency (ESA) mission *Gaia* (<https://www.cosmos.esa.int/gaia>), processed by the *Gaia* Data Processing and Analysis Consortium (DPAC, <https://www.cosmos.esa.int/web/gaia/dpac/consortium>). Funding for the DPAC has been provided by national institutions, in particular the institutions participating in the *Gaia* Multilateral Agreement. GAMA is a joint European-Australasian project based around a spectroscopic campaign using the Anglo-Australian Telescope. The GAMA input catalogue is based on data taken from the Sloan Digital Sky Survey and the UKIRT Infrared Deep Sky Survey. Complementary imaging of the GAMA regions is being obtained by a number of independent survey programmes including GALEX MIS, VST KiDS, VISTA VIKING, WISE, Herschel-ATLAS, GMRT and ASKAP providing UV to radio coverage. GAMA is funded by the STFC (UK), the ARC (Australia), the AAO, and the participating institutions. The GAMA website is <https://www.gama-survey.org/>.

APPENDIX

A. PERFORMANCE OF MLP

To assess the contribution of morphological information in our multimodal neural network, we conducted an independent performance evaluation of the MLP branch. In this test, the MLP branch used only the SED features from the KiDS dataset, which include photometry from 9-bands and 8 adjacent band colors, without integrating the morphological features processed by the CNN branch. The MLP was trained and evaluated using the same training and testing datasets as the full multimodal network. Figure 12 shows the evaluation metrics for the MLP at different output probability thresholds, analogous to Figure 3 for the full multimodal network.

The MLP achieves an overall accuracy of 97.15% on the testing dataset, with F1 scores of 96.13%, 89.90%, and 98.49% for stars, quasars, and galaxies at the default threshold. While still good, these metrics are noticeably lower than the performance of the multimodal network, especially for quasars. The MLP maintains high purity for galaxies and stars as the threshold is raised, but suffers a faster drop in completeness compared to the multimodal network. For quasars, the MLP fails to achieve both high purity and high completeness at any threshold, whereas the multimodal network can reach 99% purity with 83% completeness at $p \geq 0.99$.

These results demonstrate that the morphological information extracted by the CNN branch contributes significantly to the high performance of the multimodal network, especially when dealing with objects that are difficult to distinguish morphologically. In this way, the multimodal neural network effectively leverages complementary information from different data sources to achieve high-accuracy classification of stars, quasars, and galaxies.

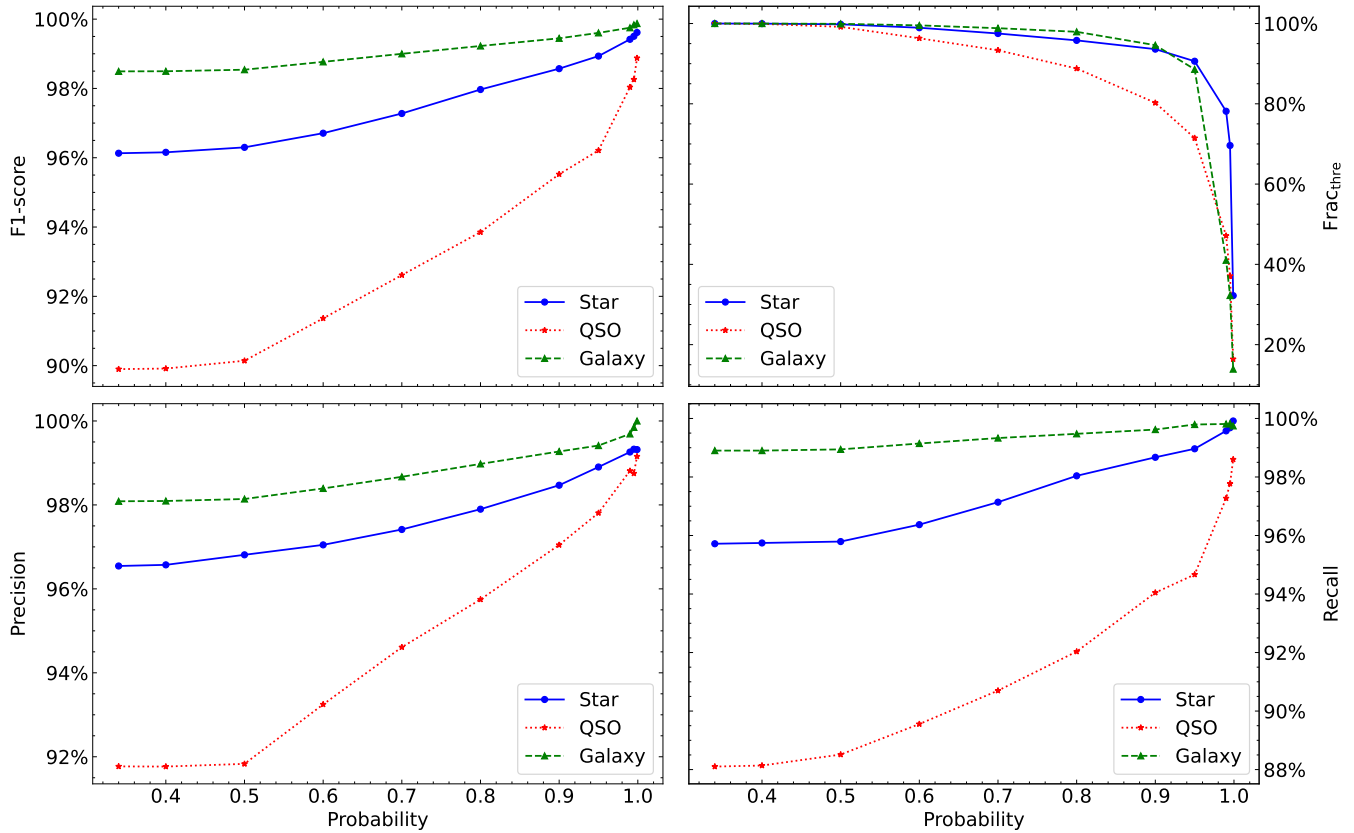


Figure 12. The same as Figure 3, but showing evaluation metrics for classification using only the MLP branch.

REFERENCES

- Abdurro'uf, Accetta, K., Aerts, C., et al. 2022, *ApJS*, 259, 35. doi:10.3847/1538-4365/ac4414
- Aihara, H., Arimoto, N., Armstrong, R., et al. 2018, *PASJ*, 70, S4. doi:10.1093/pasj/psx066
- Bai, Y., Liu, J., Wang, S., et al. 2019, *AJ*, 157, 9. doi:10.3847/1538-3881/aaf009
- Baldwin, J. A., Phillips, M. M., & Terlevich, R. 1981, *PASP*, 93, 5. doi:10.1086/130766
- Behroozi, P. S., Wechsler, R. H., & Conroy, C. 2013, *ApJ*, 770, 57. doi:10.1088/0004-637X/770/1/57
- Bolton, A. S., Schlegel, D. J., Aubourg, É., et al. 2012, *AJ*, 144, 144. doi:10.1088/0004-6256/144/5/144
- Bond, J. R., Kofman, L., & Pogosyan, D. 1996, *Nature*, 380, 603. doi:10.1038/380603a0
- Buchs, R., Davis, C., Gruen, D., et al. 2019, *MNRAS*, 489, 820. doi:10.1093/mnras/stz2162
- Cabayol, L., Sevilla-Noarbe, I., Fernández, E., et al. 2019, *MNRAS*, 483, 529. doi:10.1093/mnras/sty3129
- Capaccioli, M. & Schipani, P. 2011, *The Messenger*, 146, 2
- Capaccioli, M., Schipani, P., de Paris, G., et al. 2012, *Science from the Next Generation Imaging and Spectroscopic Surveys*, 1
- Chaini, S., Bagul, A., Deshpande, A., et al. 2023, *MNRAS*, 518, 3123. doi:10.1093/mnras/stac3336
- Conroy, C. 2013, *ARA&A*, 51, 393. doi:10.1146/annurev-astro-082812-141017
- Chen, Y. C. 2021, *ApJS*, 256, 34. doi:10.3847/1538-4365/ac13aa
- Cui, X.-Q., Zhao, Y.-H., Chu, Y.-Q., et al. 2012, *Research in Astronomy and Astrophysics*, 12, 1197. doi:10.1088/1674-4527/12/9/003
- de Jong, J. T. A., Verdoes Kleijn, G. A., Boxhoorn, D. R., et al. 2015, *A&A*, 582, A62. doi:10.1051/0004-6361/201526601
- The Dark Energy Survey Collaboration 2005, astro-ph/0510346. doi:10.48550/arXiv.astro-ph/0510346
- DESI Collaboration, Aghamousa, A., Aguilar, J., et al. 2016, arXiv:1611.00036. doi:10.48550/arXiv.1611.00036
- Dieleman, S., Willett, K. W., & Dambre, J. 2015, *MNRAS*, 450, 1441. doi:10.1093/mnras/stv632
- Driver, S. P., Hill, D. T., Kelvin, L. S., et al. 2011, *MNRAS*, 413, 971. doi:10.1111/j.1365-2966.2010.18188.x
- Driver, S. P., Bellstedt, S., Robotham, A. S. G., et al. 2022, *MNRAS*, 513, 439. doi:10.1093/mnras/stac472
- Dubois, J., Fraix-Burnet, D., Moutaka, J., et al. 2022, *A&A*, 663, A21. doi:10.1051/0004-6361/202141729

- Edge, A., Sutherland, W., Kuijken, K., et al. 2013, *The Messenger*, 154, 32
- Elvis, M., Wilkes, B. J., McDowell, J. C., et al. 1994, *ApJS*, 95, 1. doi:10.1086/192093
- Fadely, R., Hogg, D. W., & Willman, B. 2012, *ApJ*, 760, 15. doi:10.1088/0004-637X/760/1/15
- Feng, H.-C., Hu, C., Li, S.-S., et al. 2021, *ApJ*, 909, 18. doi:10.3847/1538-4357/abd851
- Fotopoulou, S., Pacaud, F., Paltani, S., et al. 2016, *A&A*, 592, A5. doi:10.1051/0004-6361/201527402
- Gaia Collaboration, Prusti, T., de Bruijne, J. H. J., et al. 2016, *A&A*, 595, A1. doi:10.1051/0004-6361/201629272
- Gaia Collaboration, Brown, A. G. A., Vallenari, A., et al. 2021, *A&A*, 649, A1. doi:10.1051/0004-6361/202039657
- Gaia Collaboration, Vallenari, A., Brown, A. G. A., et al. 2022, arXiv:2208.00211
- Gong, Y., Liu, X., Cao, Y., et al. 2019, *ApJ*, 883, 203. doi:10.3847/1538-4357/ab391e
- Guo, Z., Wu, J. F., & Sharon, C. E. 2022, arXiv:2212.07881. doi:10.48550/arXiv.2212.07881
- Han, Z., Yuan, X., Li, Z., et al. 2022, *Proc. SPIE*, 12188, 1218842. doi:10.1117/12.2637071
- He, K., Zhang, X., Ren, S., et al. 2015, arXiv:1512.03385. doi:10.48550/arXiv.1512.03385
- Helmi, A. 2020, *ARA&A*, 58, 205. doi:10.1146/annurev-astro-032620-021917
- Hubble, E. P. 1926, *ApJ*, 64, 321. doi:10.1086/143018
- Ilbert, O., Capak, P., Salvato, M., et al. 2009, *ApJ*, 690, 1236. doi:10.1088/0004-637X/690/2/1236
- Ivezić, Ž., Kahn, S. M., Tyson, J. A., et al. 2019, *ApJ*, 873, 111. doi:10.3847/1538-4357/ab042c
- Kelvin, L. S., Driver, S. P., Robotham, A. S. G., et al. 2014, *MNRAS*, 439, 1245. doi:10.1093/mnras/stt2391
- Khramtsov, V., Sergeev, A., Spiniello, C., et al. 2019, *A&A*, 632, A56. doi:10.1051/0004-6361/201936006
- Khramtsov, V., Spiniello, C., Agnello, A., et al. 2021, *A&A*, 651, A69. doi:10.1051/0004-6361/202040131
- Kormendy, J. & Ho, L. C. 2013, *ARA&A*, 51, 511. doi:10.1146/annurev-astro-082708-101811
- Kuijken, K., Heymans, C., Dvornik, A., et al. 2019, *A&A*, 625, A2. doi:10.1051/0004-6361/201834918
- Kuijken, K., Heymans, C., Hildebrandt, H., et al. 2015, *MNRAS*, 454, 3500. doi:10.1093/mnras/stv2140
- Laureijs, R., Amiaux, J., Arduini, S., et al. 2011, arXiv:1110.3193. doi:10.48550/arXiv.1110.3193
- Lecun, Y., Bottou, L., Bengio, Y., & Haffner, P. 1998, *Proc. IEEE*, 86, 2278. doi: 10.1109/5.726791.
- Li, R., Shu, Y., Su, J., et al. 2019, *MNRAS*, 482, 313. doi:10.1093/mnras/sty2708
- Li, R., Napolitano, N. R., Feng, H., et al. 2022, *A&A*, 666, A85. doi:10.1051/0004-6361/202244081
- Logan, C. H. A. & Fotopoulou, S. 2020, *A&A*, 633, A154. doi:10.1051/0004-6361/201936648
- López-Sanjuan, C., Vázquez Ramió, H., Varela, J., et al. 2019, *A&A*, 622, A177. doi:10.1051/0004-6361/201732480
- Lyke, B. W., Higley, A. N., McLane, J. N., et al. 2020, *ApJS*, 250, 8. doi:10.3847/1538-4365/aba623
- MacGillivray, H. T., Martin, R., Pratt, N. M., et al. 1976, *MNRAS*, 176, 265. doi:10.1093/mnras/176.2.265
- McCulloch, W. S., Pitts W., 1943, *Bull. Math. Biophys.*, 5, 115. doi:10.1007/BF02478259
- Nakazono, L., Mendes de Oliveira, C., Hirata, N. S. T., et al. 2021, *MNRAS*, 507, 5847. doi:10.1093/mnras/stab1835
- Peters, C. M., Richards, G. T., Myers, A. D., et al. 2015, *ApJ*, 811, 95. doi:10.1088/0004-637X/811/2/95
- Richards, G. T., Fan, X., Newberg, H. J., et al. 2002, *AJ*, 123, 2945. doi:10.1086/340187
- Salpeter, E. E. 1964, *ApJ*, 140, 796. doi:10.1086/147973
- Salvato, M., Hasinger, G., Ilbert, O., et al. 2009, *ApJ*, 690, 1250. doi:10.1088/0004-637X/690/2/1250
- Salvato, M., Wolf, J., Dwelly, T., et al. 2022, *A&A*, 661, A3. doi:10.1051/0004-6361/202141631
- Sanders, D. B., Phinney, E. S., Neugebauer, G., et al. 1989, *ApJ*, 347, 29. doi:10.1086/168094
- Schmidt, M. 1963, *Nature*, 197, 1040. doi:10.1038/1971040a0
- Scranton, R., Johnston, D., Dodelson, S., et al. 2002, *ApJ*, 579, 48. doi:10.1086/342786
- Sevilla-Noarbe, I., Hoyle, B., Marchã, M. J., et al. 2018, *MNRAS*, 481, 5451. doi:10.1093/mnras/sty2579
- Skrutskie, M. F., Cutri, R. M., Stiening, R., et al. 2006, *AJ*, 131, 1163. doi:10.1086/498708
- Smith, M. J. & Geach, J. E. 2023, *Royal Society Open Science*, 10, 221454. doi:10.1098/rsos.221454
- Szklenár, T., Bódi, A., Tarczay-Nehéz, D., et al. 2020, *ApJL*, 897, L12. doi:10.3847/2041-8213/ab9ca4
- Tadaki, K.-i., Iye, M., Fukumoto, H., et al. 2020, *MNRAS*, 496, 4276. doi:10.1093/mnras/staa1880
- Taylor, M. B. 2005, *Astronomical Data Analysis Software and Systems XIV*, 347, 29
- Verro, K., Trager, S. C., Peletier, R. F., et al. 2022, *A&A*, 660, A34. doi:10.1051/0004-6361/202142388
- Wang, T., Liu, G., Cai, Z., et al. 2023, *Science China Physics, Mechanics, and Astronomy*, 66, 109512. doi:10.1007/s11433-023-2197-5
- Wright, E. L., Eisenhardt, P. R. M., Mainzer, A. K., et al. 2010, *AJ*, 140, 1868. doi:10.1088/0004-6256/140/6/1868
- Xie, L., Napolitano, N. R., Guo, X., et al. 2023, *Science China Physics, Mechanics, and Astronomy*, 66, 129513. doi:10.1007/s11433-023-2173-8

Yang, Q. & Shen, Y. 2023, *ApJS*, 264, 9.

doi:10.3847/1538-4365/ac9ea8

Yee, H. K. C. 1991, *PASP*, 103, 396. doi:10.1086/132834

York, D. G., Adelman, J., Anderson, J. E., et al. 2000, *AJ*, 120, 1579. doi:10.1086/301513

Zhang, X., Green, G. M., & Rix, H.-W. 2023, *MNRAS*, 524, 1855.

doi:10.1093/mnras/stad1941

Zhou, X., Gong, Y., Meng, X.-M., et al. 2021, *ApJ*, 909, 53.

doi:10.3847/1538-4357/abda3e

Zuntz, J., Sheldon, E., Samuroff, S., et al. 2018, *MNRAS*, 481,

1149. doi:10.1093/mnras/sty2219